AIMS Bioengineering

AIMS Bioengineering, 13(3): 433–452.
DOI: 10.3934/bioeng.2026021
Received: 17 July 2026
Revised: 21 September 2026
Accepted: 27 September 2026
Published: 30 September 2026

https://www.aimspress.com/journal/Bioengineering

Research article

Development of a high-performance lattice cushioning system for shoe insoles

Jayesh Barve, Mohammed Irfan Khan* and Chitresh Nayak

Department of Mechanical Engineering, Medicaps University. Indore, M.P. India

* **Correspondence:** Email: dr.mohammed.irfankhan@gmail.com; Tel: +919753790113.

Abstract: All of the materials used to produce soles for traditional casual athletic shoes are nearly uniform, foam-based materials which lack any ability to regulate the long-term durability and energy absorption properties of the shoe. The recent advances of lattice-based additive manufacturing technologies have given rise to an opportunity to produce unique contoured cushioning systems that can be constructed with adjustable mechanical properties by varying the topology and porosity in a controlled manner. This research paper discusses the investigation of three types of lattice structures (i.e., gyroid, diamond, and Kelvin cell) when subjected to compressive load conditions. The lattice samples were created with four variations of porosity (i.e., 50%, 60%, 70%, and 80%) as well as two variations of thickness (i.e., 0.8 mm and 1 mm). Flexible ABS resin was produced by using the Vat photopolymerization process and the resultant samples were characterized through mechanical testing. Quasi-static loading and numerical analysis were performed on samples created using SLA technology. The results indicate that the mechanical characteristics of the three lattice types, as dictated by their topology and relative density, greatly influenced the performance of each structure; specifically, the gyroid lattice provided the best mechanical performance with the highest load resistance and the most uniform stress distribution. The diamond lattice was second to the gyroid lattice, while the Kelvin cell was found to have the lowest stiffness and failed by exhibiting signs of instability at the highest porosity levels before the other two lattice performed.

Keywords: lattice structures; TPMS lattice; gyroid; stereolithography additive manufacturing; compressive strength

Abbreviations: AM: Additive manufacturing; CAD: Computer-aided design; FEA: Finite element analysis; FEP: Fluorinated ethylene propylene; SLA: Stereolithography; TPMS: Triply periodic minimal surface; UV: Ultraviolet

1. Introduction

Customized lattice structures are deliberately designed materials where solid areas and voids are organized to attain specific mechanical properties [1]. By manipulating the topology and geometry of the void network, one can adjust useful characteristics or achieve behaviors that are seldom encountered in naturally occurring materials [2]. Lattice architectures are often classified according to the dimensional plane in which porosity is incorporated, encompassing two-dimensional configurations like honeycomb systems and fully three-dimensional structures [3]. Three-dimensional forms often include foam-like formations and triply periodic minimum surface geometries [4]. A different classification takes into account spatial distribution, differentiating between periodic lattices, stochastic networks, and functionally graded designs [5]. Engineered porous materials are progressively employed in biomedical [6], aeronautical [7], and automotive [8] applications, where regulated porosity is crucial for weight reduction, energy optimization, and multifunctional efficacy [9].

Unit cells are representative elements that are regularly repeated to construct lattice structures. When struts or beams form these unit cells, they are typically referred to as lattice structures [10], e.g. Triply periodic minimum surfaces (TPMS) and volume-based lattices. The most suitable geometries for insole applications are TPMS structures [11], especially the diamond and gyroid, because of their variable stiffness and durability [12]. Enhancing energy absorption during walking, these intricate lattice arrangements enable specific control of mechanical behavior [13]. The TPMS family comprises several lattices, including Schwartz primitive, lidinoid, IWP, gyroid, Neovius, Fischer-Koch, and diamond [14]. These structures are composed of continuous and interconnected surfaces. Because of these topological characteristics, stress concentrations are decreased, which may be advantageous for fatigue loading conditions [15].

In biological structures like the Blue-winged leafbird, Blue morpho butterfly, and Emerald-patched cattleheart butterfly, the Gyroid is a naturally occurring triply periodic minimum surface [16]. Initially characterized by Alan Schoen in 1970, it denotes a non-trivial embedded surface associated with the Schwarz minimum surface family. The gyroid is defined by its continuous curvature, lack of straight edges, and significant geometric symmetry, facilitating effective load distribution [2]. These attributes render it very appealing for lightweight, strength-constrained engineering applications. The Diamond TPMS lattice is a three-dimensional periodic architecture derived from a triply periodic minimal surface [17], meaning it forms a continuous surface with near-zero mean curvature that repeats in all spatial directions. Its geometry creates two interpenetrating but non-contacting networks separated by a smooth, continuous wall, resulting in a highly uniform distribution of material [18]. This topology eliminates sharp corners and stress concentrations, promoting efficient load transfer and isotropic mechanical behavior [19]. Because of its interconnected porosity and high surface-to-volume ratio, the diamond lattice provides an effective balance between stiffness, strength, and weight, making it suitable for lightweight structural components, energy absorption systems, and multifunctional engineered materials.

Graph-based lattices are architected cellular materials defined by a mathematical graph, where nodes represent junctions and edges represent load-bearing struts [1]. This abstraction allows precise

control over connectivity, topology, and load paths, enabling systematic tuning of stiffness, strength, and deformation behavior. The Kelvin cell is a space-filling lattice architecture derived from a truncated octahedral geometry that partitions volume with high geometric efficiency [20]. Its periodic polyhedral framework promotes uniform stress distribution and stable deformation behavior, making it a foundational model for cellular solids. Owing to its predictable stiffness–strength relationship and efficient material utilization, the Kelvin cell is widely adopted in research on lightweight lattice structures and energy-absorbing systems [21].

Additive manufacturing, more especially 3D printing [22], has dominated recent orthotic insole research [23,24]. Typically, the design of architected cellular materials necessitates intricate geometries and forms that are challenging to produce using traditional manufacturing techniques [25]. Consequently, additive manufacturing presents itself as a promising alternative for the production of cellular materials. This collection of manufacturing techniques constructs objects featuring intricate 3D shapes through a systematic layer-by-layer approach [26]. Among the various additive manufacturing technologies, VAT Photopolymerization stands out as the most favoured option, primarily attributed to its straightforward nature and cost-effectiveness [27]. Vat photopolymerization is an additive manufacturing process in which a liquid photopolymer resin is selectively cured using a light source, typically ultraviolet (UV) radiation, to form solid layers in a layer-by-layer manner [28]. A build platform incrementally moves to allow successive curing of cross-sectional geometries derived from a digital model. This technique enables high resolution, smooth surface finish, and precise feature control, making it suitable for complex geometries and intricate lattice structures. It widely applied in biomedical, dental, microstructural, and prototyping applications [29].

In this work, we offer the thorough examination of the three lattice configurations for compressive evaluation of shoe insole cushioning material. In addition to discussing the impact of porosity, the work uses experimental and numerical testing to investigate compressive strength. Additionally, a separate porosity trend is formed, emphasizing mechanical strength fluctuations. Previous studies have demonstrated the potential of lattice architectures for footwear and orthotic applications; however, direct experimental comparisons among TPMS and conventional cellular topologies under identical material, specimen size and manufacturing conditions remain limited. In particular, the coupled effects of topology, porosity and wall thickness on the quasi-static compression response of SLA-manufactured Gyroid, Diamond and Kelvin-cell structures have not been systematically compared within a common experimental and numerical framework. Therefore, the present study evaluates these three architectures under identical manufacturing and testing conditions to establish comparative relationships among geometric parameters, stiffness, compressive strength, deformation behaviour and energy absorption. The results are intended to provide architecture-level design guidance for subsequent development and validation of lattice-based cushioning systems.

2. Materials and methods

The comprehensive technique employed in this study is encapsulated in Figure 1. The design procedure for the lattice insoles cushioning commenced with the selection of the application. Utilizing nTopology's implicit modeling design software, all three lattice structures were engineered based on porosity and thickness. The lattice cushioning utilized in the insole was modeled and incorporated into the insole design. Finite element analyses of various lattice structures for compressive behavior models

were conducted to characterize deformation and Von Mises stresses under applied pressures. Ultimately, chosen lattices were produced by additive manufacturing utilizing stereolithography.

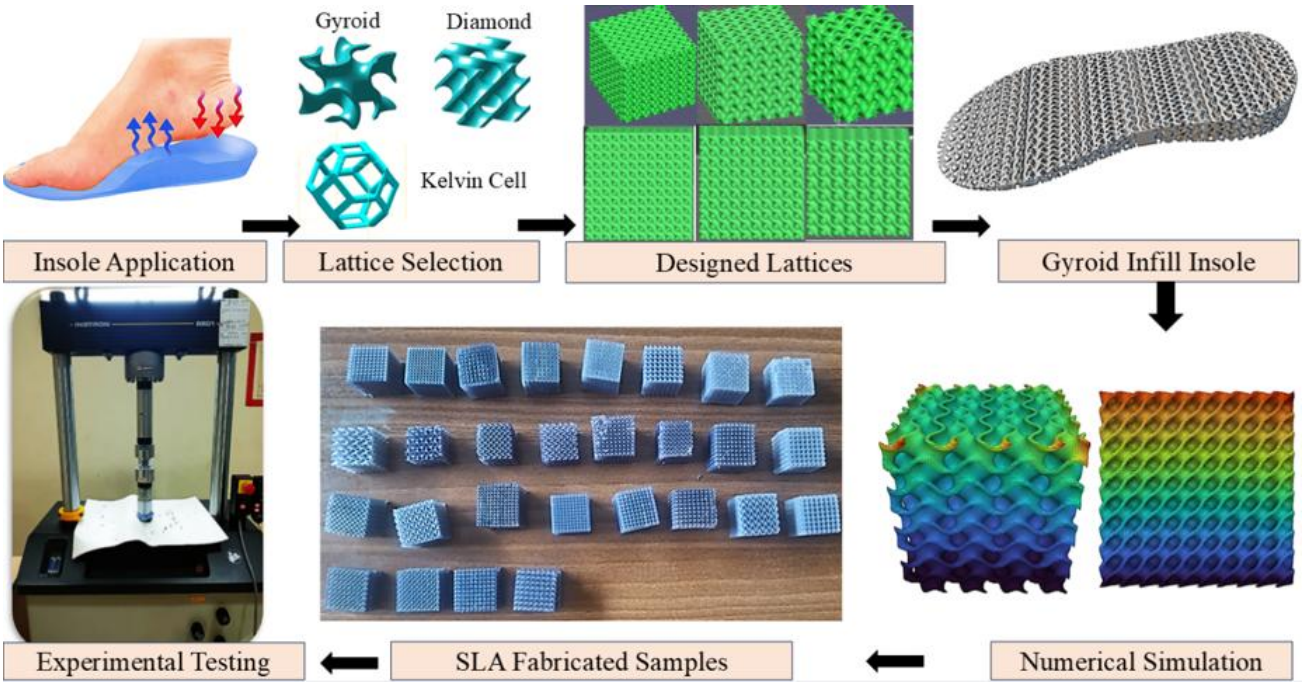


Figure 1. Adopted methodology: insole modelling, unit cells, Lattice designs, Printed samples, modelling, and Quasi static testing.

2.1. Design of lattices

The lattice architectures (Gyroid, Diamond, and Kelvin cell) were modelled using nTopology software with four porosity levels (50%, 60%, 70%, and 80%) and two wall thickness configurations (0.8 mm and 1 mm). The unit cell size was systematically adjusted to achieve the targeted porosity levels. For instance, in the Diamond lattice, the unit cell size increased from 4.15 mm at 50% porosity to 4.54 mm at 60% and 4.91 mm at 70% porosity. Correspondingly, the surface area exhibited a proportional increase with porosity, measuring 4001.3 mm² (50%), 4802.3 mm² (60%), and 5606.2 mm² (70%). Each optimized unit cell was mapped and periodically replicated within a 20 × 20 × 20 mm cubic domain to generate the final lattice specimens. The mass and volume value has been shown in Table 1 obtained from ntopology software according to different unit cell size.

Table 1. Design parameter details of three lattices as per wall thickness, porosity and unit cell sizes.

		Wall thickness (0.8mm)			Wall thickness (1 mm)		
Structure	Porosity (%)	Unit cell size (mm)	Mass (g)	Volume (mm^3)	Unit cell size (mm)	Mass (g)	Volume (mm^3)
Diamond	50%	4.15	4.33	4001.3	5.13	4.28	3982.4
	60%	4.54	5.19	4802.3	4	5.158	4810.4
	70%	4.91	6.055	5606.2	4.34	6.125	5602.3
	80%	3.99	6.92	6408	3.45	6.9	6399.8
Gyroid	50%	3.45	4.335	4014.2	3.55	4.86	3917.2
	60%	3.8	5.25	4860.2	3.76	5.45	4720.3
	70%	5.24	6.086	5601	5.23	6.21	5442.1
	80%	2.82	6.905	6399.9	2.72	6.99	6119.2
Kelvin	50%	2.58	4.32	4008.07	2.55	4.44	3898.05
	60%	2.81	4.9	4799.8	2.77	5.04	4655.8
	70%	2.11	6.035	5590.2	2.1	6.115	5350.2
	80%	1.94	6.9	6398.9	1.88	6.81	6296.1

2.2. Simulation framework

The numerical compression analysis was performed in nTopology using a linear static structural framework. The photopolymer resin was represented using a linear isotropic elastic constitutive model. The static simulation was meticulously crafted to accurately emulate the conditions of the experimental compression test by the application of suitable boundary constraints. The lower surface of the lattice structure was completely constrained, whilst the upper surface experienced a steady downward velocity of 1.5 mm/min, imitating compressive force. The upper limit was presumed to exhibit no lateral or longitudinal displacements, therefore preventing any inadvertent movement during deformation. Contact between the loading surface and specimen was assumed to be frictionless, and the analysis was conducted under a small-deformation assumption without geometric nonlinearity. Each lattice structure was discretized using a refined finite element mesh, with additional refinement implemented to precisely capture stress distribution, especially the von Mises stress. The lattice geometry was discretised using three-dimensional tetrahedral solid finite elements. The minimum element size varied between 0.25 and 0.5 mm, yielding 372,602 mixed elements and 75,535 nodes in the final mesh.

2.3. Stereolithography manufacturing of Lattices

Prior to issuing the print order to the SLA 3D printer, multiple pre-processing procedures were executed to minimize the likelihood of sample failure. In the pre-processing phase, the initial step involved orienting the sample on the machine platform, either vertically, horizontally, or at an incline. Our research employs a horizontal build orientation. The build orientation can affect layer adhesion, dimensional accuracy, and the anisotropy of the printed specimen. The subsequent phase in pre-processing is the cleaning and leveling of the build platform. The resin was filtered to remove

particulate contaminants, and the FEP film was checked to ensure that it was properly tensioned before printing.

Table 2. Material and SLA 3D printing used to manufacture the samples [30–32].

Flexible ABS resin properties	Values	SLA parameters	Value
Polymer density (g/cm^3)	1.15	Layer height (mm)	0.05
Shore hardnes	70D	Exposure time (sec)	7
Tensile strength (MPa)	28	Bottom exposure time (sec)	60
Young modulus (MPa)	800	Bottom lift distance (mm)	5
Heat distortion temperature	55 °C	Bottom lift speed (mm/min)	65
Elongation at break (%)	70	Retract speed (mm/min)	150



Figure 2. Adopted SLA manufacturing: Machine with selected flexible material, and post processing (washing and curing).

The Creality HALOT Mage S 14K SLA Printer is utilized for specimen printing, with a maximum print volume of 223 × 126 × 230 mm, a printing speed of 150 mm/h, and a maximum resolution for surface finish. Siraya Tech FAST ABS flexible 3D printer resin, 405nm UV-curing, serves as the base material. Delivering non-brittle, high-precision materials with reduced volumetric shrinkage, elevated tensile strength, and appropriate modulus of elasticity. Table 2 shows the selected property of resin and SLA 3D printer [31–33]. The G-code input is utilized in the simultaneous preparation of four samples. The cumulative duration for printing the four examples is 40 minutes, necessitating 211 layers for completion. The printed samples did not employ the support system during the printing process due to used lattices are self-supported nature. Figure 2 presents the SLA additive manufacturing steps to built flowless samples.

2.4. Quasi static testing

The quasi-static test configuration, the tested samples, and the performance results for the chosen Gyroid, Diamond, and Kelvin cell architectures are shown in Figure 3. A total of 24 samples were

tested: eight samples from each lattice, corresponding to four porosities and two thicknesses of 0.8 and 1 mm. The samples underwent a compression test using the Instron 8801 material strength measurement apparatus, which features a hydraulic pressure supply of 207 bar, an actuator stroke of 150 mm, and a load capacity of 100 kN. The test was conducted at room temperature with an initial displacement rate of 1.5 mm/min, utilizing the wave matrix-2 dynamic testing software for accurate control.

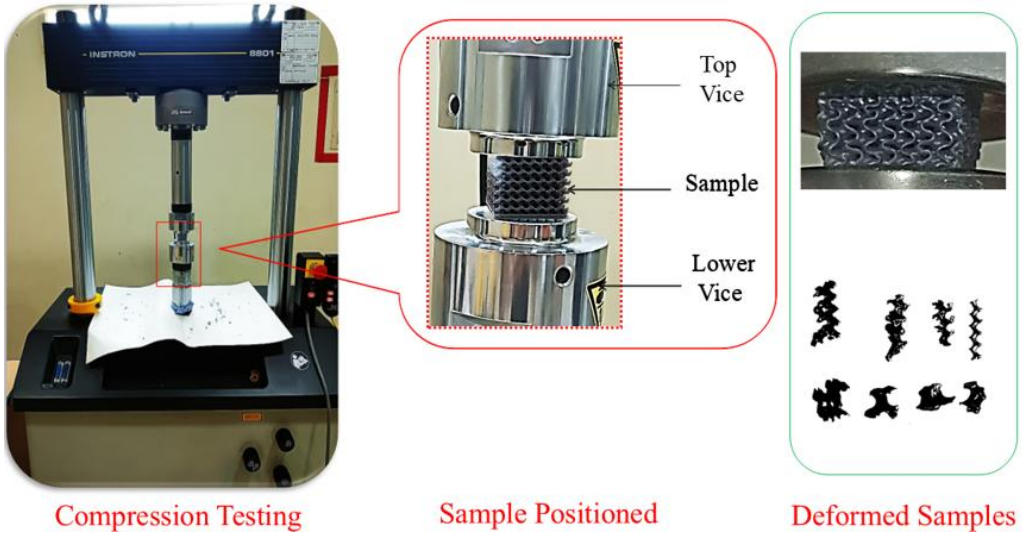


Figure 3. Testing setup and deformed sample and patterns.

The mechanical performance of the lattice structures was further quantified in terms of effective elastic modulus, volumetric energy absorption, specific energy absorption, plateau stress, and densification strain. The volumetric energy absorption W was calculated as the area under the experimental stress-strain curve up to the densification strain εD:

$$W = \int_0^{\varepsilon D} \sigma(\varepsilon) d\varepsilon \tag{1}$$

The specific energy absorption was calculated by normalising the volumetric energy absorption by the measured lattice density:

$$SEA = \frac{W}{\rho^*} \tag{2}$$

where ρ* is the experimentally measured apparent density of the printed lattice. SEA may be reported in J kg^{-1} or kJ kg^{-1}.

The effective elastic modulus E^* was calculated from the slope of the initial approximately linear portion of the experimental stress-strain curve:

$$E^* = \frac{\Delta\sigma}{\Delta\varepsilon} \tag{3}$$

where Δσ and Δε are the changes in compressive stress and strain, respectively. The same initial strain interval was used for all lattice configurations to ensure consistent comparison.

3. Results and discussion

This section presents the mechanical performance evaluation of Gyroid, Diamond, and Kelvin cell lattice structures designed and manufactured with varying porosity and wall thickness parameters. Quasi-static compression tests were conducted to assess their load-bearing capacity, stiffness, and energy absorption behavior. The experimental investigation enables a comparative analysis of structural response as a function of geometric configuration and material distribution.

3.1. Stress-strain response

Figure 4A illustrates that the Gyroid lattice demonstrates a mechanical response that is distinctly depending on porosity. The 50% porosity configuration exhibits the greatest compressive strength, with around 2.473 MPa, closely succeeded by the 60% specimen at around 2.27 MPa. As porosity escalates to 70% and 80%, the peak stress markedly diminishes to around 0.9 MPa and 0.8 MPa, respectively. The lower-porosity samples exhibit a consistent strain-hardening phase before densification, while higher-porosity structures demonstrate early plateau behavior with diminished load-bearing capability. Reducing porosity significantly improves stiffness and maximum compressive strength in the Gyroid structure.

Figure 4B illustrates The Diamond lattice exhibits a comparable pattern, with the 50% porosity specimen attaining the maximum compressive strength of 1.859 MPa. The 60% configuration achieves around 1.313 MPa, but the 70% and 80% porosity samples demonstrate reduced peak stresses of roughly 0.9 MPa and 0.8 MPa, respectively. In comparison to the Gyroid, the Diamond lattice exhibits somewhat reduced maximum stress values while preserving a rather smooth stress-strain trajectory. The decline in strength with increasing porosity is consistent, demonstrating a pronounced sensitivity of this topology to material fraction.

Figure 4C illustrates that the Kelvin cell exhibits relatively lower peak stresses at all porosity levels. The structure with 50% porosity attains roughly 1.17 MPa, whereas the 60% porosity structure achieves around 1.15 MPa. The 70% and 80% samples have peak stresses of around 1.0 MPa and 0.6 MPa, respectively. Despite the Kelvin lattice demonstrating stable deformation and extensive plateau zones, its total compressive strength is inferior to that of the Gyroid and Diamond structures, especially at reduced porosity levels.

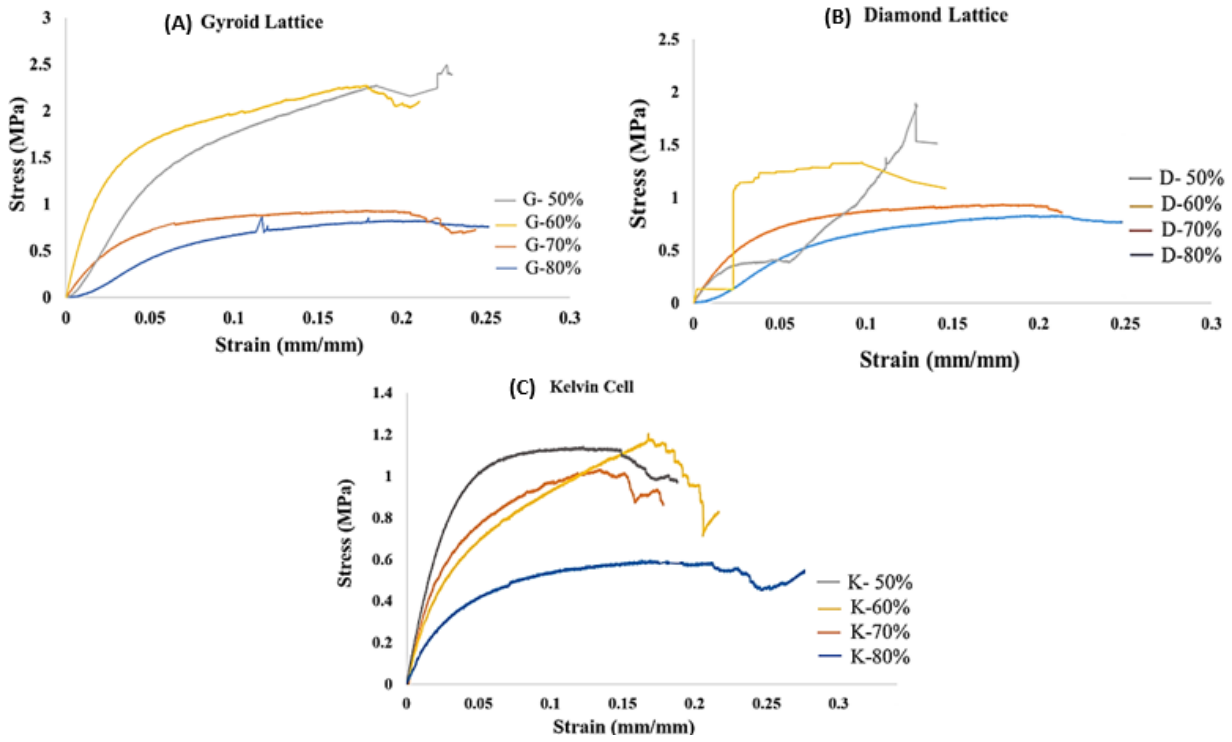


Figure 4. Stress-strain porosity based experimental results for Gyroid, Diamond and Kelvin Cell lattice structures (0.8mm thickness).

3.1.1. Comparative analysis and percentage variations

For the 0.8 mm wall thickness, the Gyroid lattice exhibited the highest peak compressive stresses at 50% and 60% porosity, reaching approximately 2.47 and 2.27 MPa, respectively. The corresponding Diamond values were approximately 1.86 and 1.31 MPa, whereas the Kelvin-cell values were approximately 1.17 and 1.15 MPa. At higher porosity levels, the differences between the three topologies became less pronounced. The Gyroid lattice at 50% porosity results surpassing the Diamond lattice by around 26–30% and the Kelvin cell by nearly 50–52%. At 60% porosity, the Gyroid exhibits exceptional performance, with approximately 40% greater strength than Diamond and almost 80% greater than Kelvin.

3.1.2. Energy absorption behaviour

Energy absorption, derived from the region beneath the stress–strain curves, exhibits tendencies analogous to compressive strength. The Gyroid lattice at 50% and 60% porosity demonstrates optimal energy absorption owing to its increased stress levels coupled with prolonged strain hardening before densification. The significant plateau stress and postponed failure enhance energy dissipation capability. The Diamond lattice exhibits significant energy absorption, especially at 50% porosity; nevertheless, the premature commencement of stress reduction at elevated porosities constrains its total absorbed energy relative to the Gyroid structure. The Kelvin cell, albeit demonstrating reduced peak stresses, displays relatively prolonged plateau areas at intermediate porosities (60–70%), resulting in stable yet comparatively diminished total energy absorption. At 80% porosity, all three

lattices exhibit a substantial decrease in absorbed energy due to reduced material fraction and premature structural failure.

Figure 5A illustrates the results for 1mm thickness lattices. The gyroid lattice demonstrates superior compressive performance compared to the other two configurations. The samples with 50% and 60% porosity exhibit enhanced load-bearing capacity, attaining maximum stresses of around 6.2 MPa (50%) and 6.0 MPa (60%). Both exhibit a stable deformation zone succeeded by progressive softening post-densification. The 70% sample exhibits moderate strength (about 4.6 MPa), whereas the 80% structure registers the lowest peak stress (around 4.4 MPa). A distinct decrease in stiffness and peak stress is noted with rising porosity, suggesting that diminished porosity improves structural rigidity and load transfer efficacy in the gyroid topology.

Figure 5B illustrates that the diamond lattice has relatively inferior strength compared to the gyroid, however retains commendable deformation stability. The sample with 50% porosity attains the maximum peak stress of approximately 4.8 MPa, succeeded by the 60% porosity sample at around 4.6 MPa. The 70% lattice attains roughly 2.8 MPa, whilst the 80% structure has the lowest strength at approximately 1.9 MPa. The stress-strain curves demonstrate incremental layer-by-layer failure, particularly at elevated porosities, leading to diminished stiffness and energy absorption capability.

Figure 5C illustrates that the Kelvin cell lattice exhibits intermediate characteristics between gyroid and diamond structures. The sample with 50% porosity attains a peak stress of roughly 4.5 MPa, succeeded by the 60% sample at approximately 4.0 MPa. The samples at 70% and 80% exhibit markedly diminished strengths of around 2.6 and 1.6 MPa, respectively. The Kelvin structure demonstrates a gradual elastic-plastic transition accompanied by significant densification at elevated strains. Like other lattices, enhanced porosity diminishes stiffness and load-bearing capability.

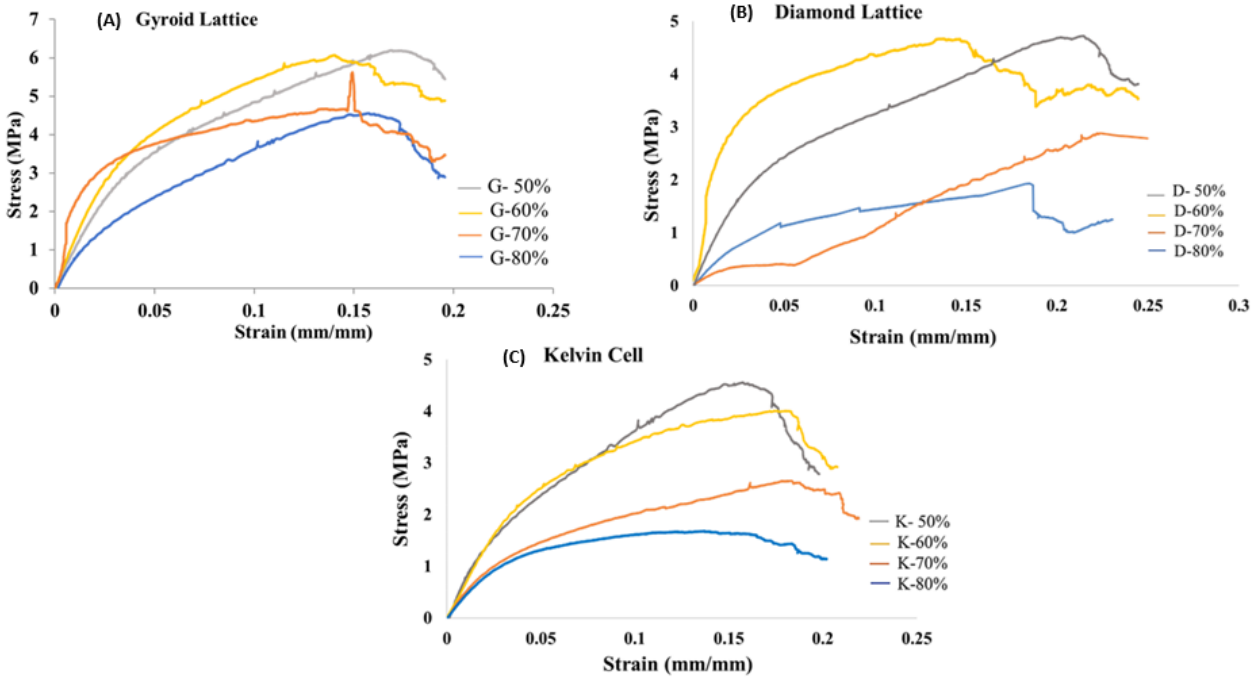


Figure 5. Stress-strain porosity based experimental results for Gyroid, Diamond and Kelvin Cell lattice structures (1 mm thickness).

3.1.3. Comparative analysis and percentage variations

The gyroid lattice with 50% porosity surpasses the diamond lattice by roughly 29% and the Kelvin cell by approximately 38% regarding peak compressive strength. Furthermore, diamond has around 7% greater strength than the Kelvin structure. Reduced porosity (50–60%) consistently yields enhanced stiffness and load-bearing capability across all three lattice configurations.

3.1.4. Energy absorption behaviour

The energy absorption behavior (area under the stress-strain curve) follows a similar trend to the peak stress results. For all three lattice types, the 50% and 60% porosity structures exhibit significantly higher energy absorption due to their higher load-bearing capacity and extended plateau region before densification. Among them, the Gyroid lattice at 50–60% porosity shows the highest energy absorption, owing to its smooth stress distribution and continuous deformation mechanism. The Diamond lattice demonstrates moderate energy absorption, particularly at 50% porosity, while the Kelvin cell shows comparatively lower absorption because of earlier stress softening and reduced peak stress.

In terms of stiffness (initial slope of the stress-strain curve), the Gyroid lattice exhibits the highest stiffness, followed by the Diamond lattice, and then the Kelvin cell. Stiffness decreases consistently with increasing porosity (from 50% to 80%) across all lattice types due to reduced solid volume fraction and thinner load paths.

3.2. Simulation analysis results

Figure 6 illustrates the results for low and high porosity gyroid lattices, exhibiting a similar general mechanical trend, although revealing significant disparities in peak stress levels, deformation behaviour, and densification response. Improved load-bearing capacity and progressive collapse behavior are indicated by the lattice structure's comparatively higher peak stress and more stable plateau region in the first result. The second result demonstrates relatively lower peak stress and earlier softening, indicating diminished stiffness and compromised structural integrity under compressive loading. The disparity between the two arises from differences in lattice topology and internal load distribution mechanisms, with one structure facilitating more continuous stress transfer paths, while the other experiences localized deformation. Both results show porosity's effect. Peak stress, stiffness, and energy absorption capacity decrease as porosity increases from 50–60% to 70–80%. Higher solid volume fractions in lower porosity structures result in thicker struts or walls and better deformation resistance. They have higher initial stiffness (steeper elastic slope) and energy absorption due to delayed densification. Higher porosity structures have lower relative density, thinner load paths, earlier structural collapse, and lower mechanical performance. Thus, porosity controls stiffness, strength, and cushioning, with moderate porosity balancing lightweight design and mechanical efficiency.

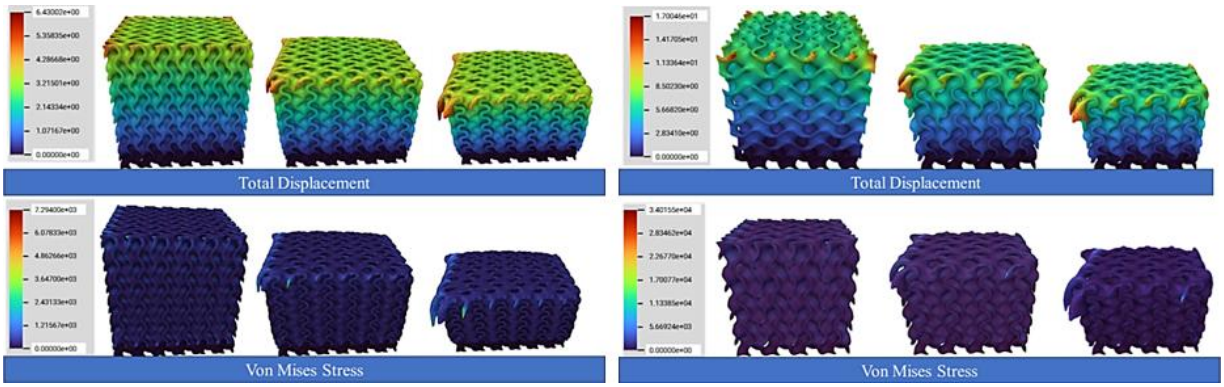


Figure 6. Finite element model of a gyroid lattice at higher and lower porosity at 0.8mm thickness and at a 0% compression, b 25% compression, and c 50% compression.

The simulation results for the diamond lattice with a strut thickness of 0.8 mm, as depicted in Figure 7, demonstrate a distinct correlation between deformation and stress distribution relative to porosity. The total displacement contours indicate that the highest displacement occurs in the structure with greater porosity, whereas the sample with lower porosity demonstrates significantly reduced deformation under identical loading conditions. This signifies that reduced porosity improves structural rigidity and compressive load resistance.

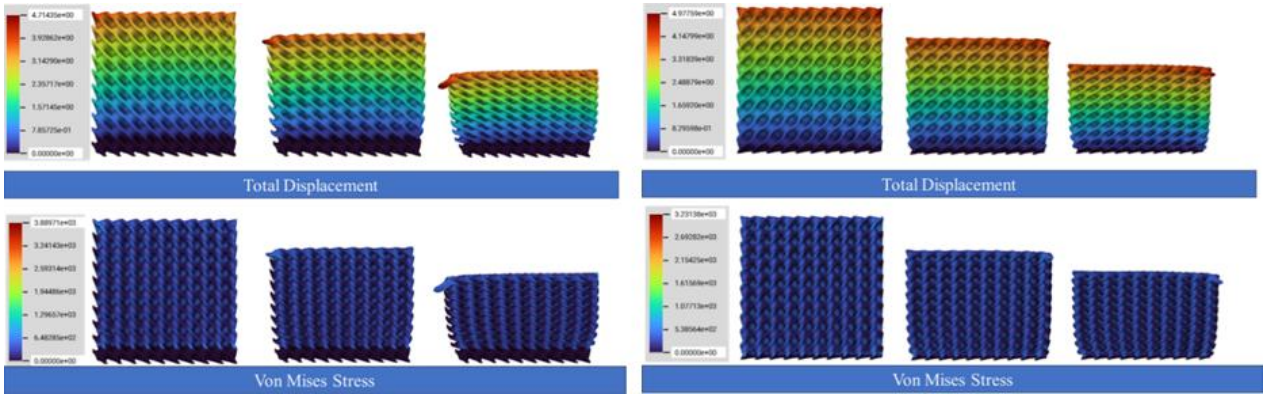


Figure 7. Finite element model of a diamond lattice at higher and lower porosity at 0.8mm thickness and at a 0% compression, b 25% compression, and c 50% compression.

This pattern is in agreement with the gyroid lattice results that were previously discussed, which showed a noticeable decrease in peak stress, stiffness, and energy absorption when porosity increased from 50% to 80%. In both topologies, structures with lower porosity (50–60%) demonstrate reduced deformation, enhanced stress distribution, and superior structural rigidity attributable to increased relative density and more robust load paths. When directly compared, the gyroid lattice exhibited superior mechanical performance compared to the diamond lattice at equivalent porosity levels. The gyroid structure exhibited superior peak compressive strength and enhanced energy absorption capacity, attributable to its continuous smooth surface geometry that facilitates uniform stress distribution and postpones localized failure.

The Kelvin cell lattice under compressive loading exhibits a progressive and relatively uniform deformation pattern across different porosity levels in Figure 8. From the total displacement contours, it is observed that displacement increases with increasing porosity, indicating a reduction in stiffness and structural rigidity. The lower porosity configuration shows smaller vertical deformation and a more compact structure, confirming higher resistance to compression. In contrast, higher porosity samples demonstrate greater axial shortening and more pronounced layer-wise deformation. The Von Mises stress distribution indicates that stresses are primarily concentrated at the strut junctions and along the vertical load paths. In lower porosity Kelvin structures, stress is more uniformly distributed across the network, suggesting efficient load transfer. As porosity increases, stress magnitude decreases due to reduced material volume, but localized stress concentrations become more visible at nodal connections, which may initiate early structural collapse. The deformation pattern of the Kelvin lattice is characterized by a bending-dominated mechanism, where struts gradually buckle and collapse in a relatively symmetric manner. When compared with the previously analyzed gyroid and diamond lattices, the Kelvin cell exhibits comparatively lower stiffness and peak stress at similar porosity levels. The gyroid lattice demonstrated the most uniform stress distribution and the highest load-bearing capacity due to its continuous smooth geometry, which delays localized failure. The diamond lattice showed intermediate behaviour, with moderate stiffness and noticeable stress concentration at nodal junctions.

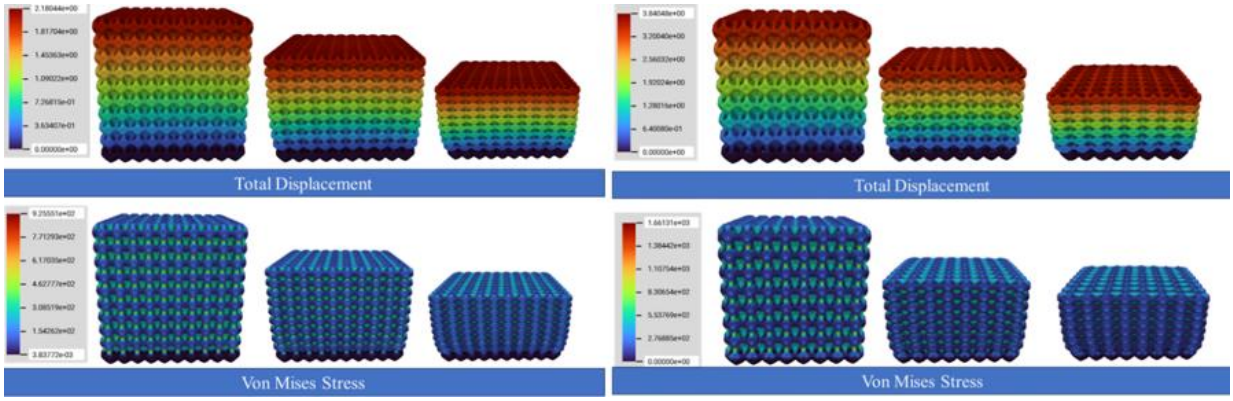


Figure 8. Finite element model of a kelvin cell lattice at higher and lower porosity at 0.8mm thickness and at a 0% compression, b 25% compression, and c 50% compression.

3.3. Experimental deformation behaviour of Lattices

The progressive collapse mechanism of the lattice structures at 50% and 70% porosity is clearly illustrated by the deformation images taken at 0%, 25%, and 50% compressive strain in Figure 9. At 0% strain, the structures retain their original geometry without distortion. At 25% strain, axial shortening and slight lateral expansion are observed, indicating the onset of bending-dominated deformation, with the 70% porosity sample exhibiting greater instability due to lower stiffness. At 50% strain, significant layer-by-layer buckling and densification occur, with the higher porosity structure showing more pronounced lateral bulging and non-uniform collapse, while the 50% porosity sample maintains comparatively more controlled and stable deformation. Overall, increasing porosity leads to earlier instability and greater compressive.

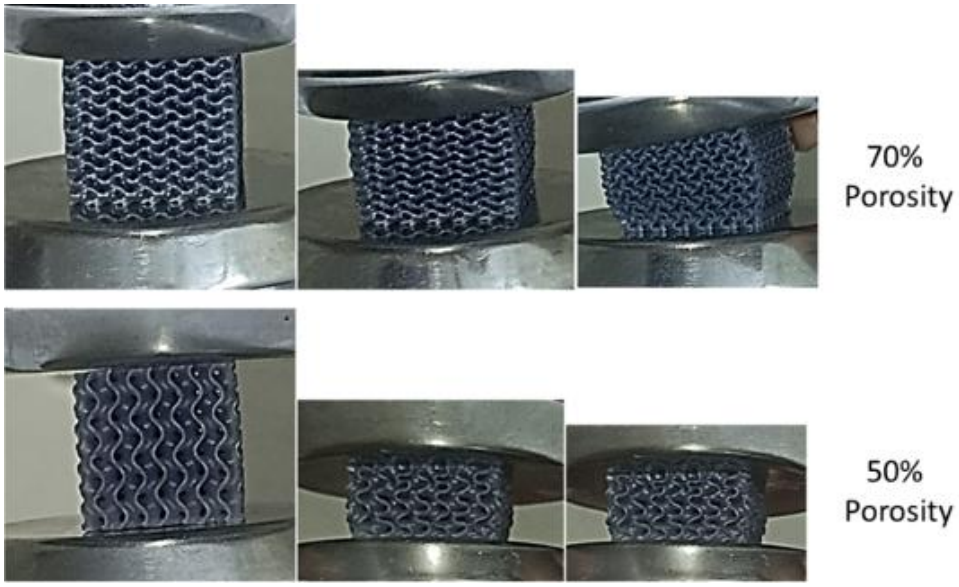


Figure 9. Deformation patterns for gyroid lattice in compressive testing.

Figure 10 illustrates the compressive deformation images for the diamond lattice at 50% and 70% porosity, highlighting a progressive collapse mechanism as strain increases. In the preliminary phase, both structures maintain their geometric integrity. As compression intensifies, there is a clear occurrence of axial shortening accompanied by significant lateral bulging, suggesting a deformation pattern that is primarily dominated by bending. The sample with 70% porosity exhibits earlier instability, increased lateral expansion, and more significant non-uniform deformation, attributed to its lower relative density and diminished stiffness. Conversely, the lattice with 50% porosity demonstrates superior structural alignment and shows a more regulated, layer-by-layer collapse prior to densification. In summary, reduced porosity contributes to improved compressive stability, whereas increased porosity results in premature buckling and greater deformation.

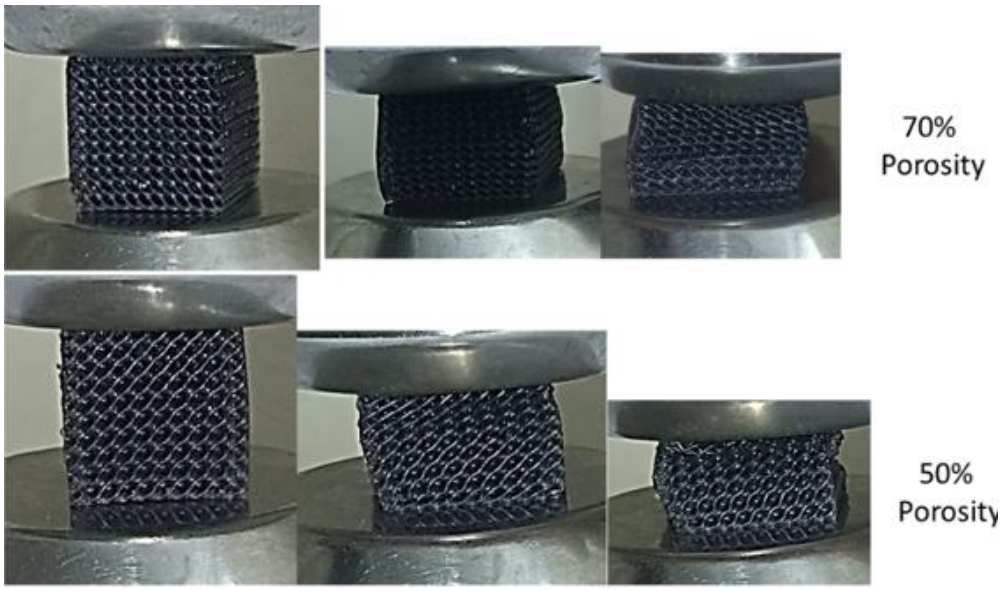


Figure 10. Deformation patterns for diamond lattice in compressive testing.

Figure 11 illustrates the compressive deformation images of the Kelvin cell lattice at 50% and 70% porosity, revealing a unique deformation mechanism in contrast to the previously examined gyroid and diamond lattices. In the early phase, the structure maintains geometric stability; yet, as compression intensifies, the Kelvin lattice demonstrates increasingly noticeable bending and nodal buckling characteristics. The deformation advances via a methodical layer-by-layer compaction, characterized by the noticeable crushing of cell junctions instead of a uniform surface collapse. The sample with 70% porosity exhibits earlier lateral bulging, increased axial shortening, and greater localized instability as a result of its lower relative density. The structure with 50% porosity exhibits a more regulated deformation process, accompanied by a postponement of densification.

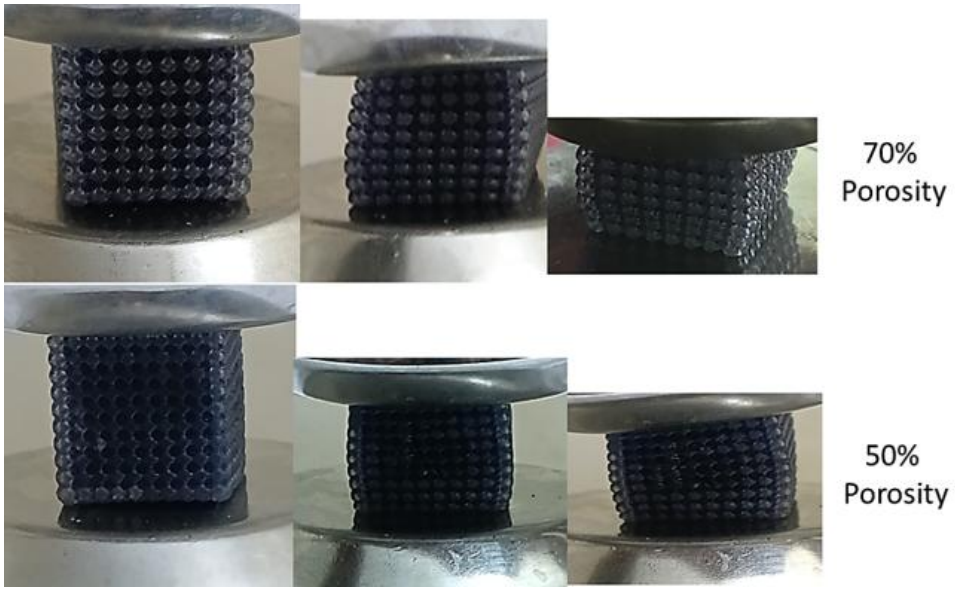


Figure 11. Deformation patterns for Kelvin cell lattice in compressive testing.

Compared to the gyroid lattice, which shows smooth and uniform continuous deformation, the Kelvin cell exhibits more discrete and localized buckling due to its strut-based geometry. Relative to the diamond lattice, the Kelvin structure displays more evident nodal collapse and slightly less uniform stress distribution.

3.4. Empirical relation based on mechanical performance for shoe insole cushioning

From the observed results, compressive strength, stiffness, and energy absorption decrease with increasing porosity due to reduction in solid volume fraction. The mechanical response of lattice structures can be expressed using a Gibson–Ashby type power-law relation [33]:

$$\sigma^* = C_1 \sigma_S \left(\frac{\rho^*}{\rho_S}\right)^n \tag{4}$$

$$E^* = C_2 E_S \left(\frac{\rho^*}{\rho_S}\right)^m \tag{5}$$

In the above relations, $\sigma*$ represents the compressive strength of the lattice structure, while E^* denotes the effective elastic modulus or stiffness of the lattice. The terms σ_s, and E_s correspond to the

intrinsic mechanical properties of the fully dense solid material. The ratio ρ^*/ρ_s defines the relative density of the lattice, which is equal to (1-Porosity), indicating the fraction of solid material present in the structure. The constants $C1$ and $C2$ are geometry-dependent coefficients that vary according to lattice topology (e.g., gyroid, diamond, or Kelvin cell). The exponents n and m describe the deformation mechanism of the lattice and typically range between 1.5 and 2 for bending-dominated cellular structures.

Because the Gyroid lattice showed the highest strength and energy absorption at 50–60% porosity, it suggests a more efficient stress distribution and stable collapse mechanism compared to Diamond and Kelvin structures.

In shoe insole cushioning applications, the primary design objective is to achieve an optimal balance between high energy absorption for impact protection, moderate stiffness for comfort and flexibility, and a lightweight structural configuration. Based on the experimental results, lattice porosity plays a critical role in tailoring these properties. A 50% porosity gyroid lattice exhibits higher stiffness and superior impact resistance, making it particularly suitable for the heel region where maximum ground reaction forces occur during walking or running. Increasing the porosity to 60–70% provides moderate stiffness with enhanced cushioning behaviour, which is ideal for the midfoot region that requires a balance between support and comfort. At higher porosity levels (70–80%), the lattice structure demonstrates a softer mechanical response, improving flexibility and adaptability in the forefoot region. Therefore, a functionally graded gyroid lattice insole with spatially varying porosity can effectively distribute loads, reduce peak plantar pressure, and enhance overall comfort and shock absorption performance. The study confirms that topology selection (Gyroid) combined with controlled porosity (50–60%) provides represents a promising candidate for further investigation in lattice-based cushioning applications manufactured via additive manufacturing.

From an engineering-design perspective, the observed differences suggest that spatially graded lattice architectures may offer a route for tailoring local stiffness in future insole designs. However, the present coupon-level experiments do not establish regional plantar-pressure reduction, comfort or clinical performance. Such application-level conclusions require full-insole manufacturing followed by cyclic compression, dynamic loading and plantar-pressure validation.

4. Conclusion

In this work, SLA 3D printing was used to design and create insoles featuring lattice architectures. The compressive behavior of the gyroid, diamond, and kelvin cell produced samples was examined. The various thicknesses and porosities were examined. The present investigation was performed using 20 × 20 × 20 mm lattice coupons under quasi-static compression and therefore represents an architecture-screening study rather than validation of a complete orthotic insole. The results establish relationships between topology, porosity, wall thickness and compressive behaviour that can guide subsequent insole design. However, direct conclusions regarding plantar-pressure reduction, user comfort or regional heel-midfoot-forefoot performance require validation using full-scale insoles, cyclic loading, dynamic impact testing and plantar-pressure measurements. The primary findings from this study were

- Among the optimal configurations (50% porosity), the Gyroid lattice outperformed Diamond and Kelvin structures, making it the most suitable topology for applications requiring high energy absorption and load-bearing efficiency.

- The mechanical performance of all three lattice structures is strongly influenced by porosity, with lower porosity (50–60%) providing superior compressive strength, stiffness, and energy absorption.
- The study concludes that appropriate topology selection, particularly the Gyroid lattice, combined with controlled porosity in the range of 50–60%, provides an optimal balance between cushioning and structural support. This combination offers superior energy absorption, adequate stiffness, and lightweight characteristics, making it highly suitable for advanced lattice-based shoe insole applications fabricated through additive manufacturing.
- Based on the simulation analysis, the Gyroid lattice at lower porosity (50–60%) demonstrated the most stable and uniform deformation pattern, along with the highest load-bearing capacity and energy absorption, positioning it as the best-performing configuration under compressive loading.
- The Kelvin lattice exhibits greater sensitivity to porosity variations and demonstrates earlier structural instability at higher porosity levels, whereas the Gyroid lattice maintains the most stable, uniform, and controlled compressive deformation among the three investigated topologies.

The present study is limited to single cubic lattice specimens tested under quasi-static compression, without replicate testing or full-scale insole validation. Manufacturing-induced deviations in actual porosity and wall thickness were also not quantified. Future work should include replicate testing, dimensional/porosity measurements, cyclic and dynamic loading, and full-insole plantar-pressure evaluation to validate the proposed cushioning performance.

Use of AI tools declaration

The authors declare they have not used Artificial Intelligence (AI) tools in the creation of this article.

Acknowledgement

The authors gratefully acknowledge the financial support provided by Medicaps University, Indore, under the Seed Money Project (SMPS)/ No. 26 Dated 23/06/2023 for the research project entitled “Design and Development of customised anatomical Fit foot insoles by integrating Additive Manufacturing and Reverse Engineering.” The authors sincerely acknowledge the University’s support and resources, which contributed to the successful completion of the research work presented in this paper.

Availability of data and materials

On request, the corresponding authors will provide all information and materials necessary to produce the findings in this study.

Conflict of interest

The authors declare no conflict of interest.

Author contributions

Jayesh Barve: Conceptualization, methodology, software, investigation, formal analysis, data curation, visualization, writing—original draft.

Mohammed Irfan Khan: Conceptualization, supervision, methodology, validation, interpretation of results, writing—review and editing, project administration, and overall guidance of the research and corresponding author.

Chitresh Nayak: Investigation, experimental validation, resources, data curation, and writing—review and editing.

All authors have read and approved the final version of the manuscript and agree to be accountable for all aspects of the work.

References

1. Liu F, Shao Y, Chen M (2026) Generative design strategies for additive manufacturing of lattice structures: a review. *Mater Des* 262: 115431. https://doi.org/10.1016/j.matdes.2026.115431
2. Zimmerman BK, Carlton HD, Lind J, et al. (2026) Investigating property-porosity relationships for micro-architected lattice structures. *Sci Rep* 16: 5521. https://doi.org/10.1038/s41598-026-35262-6
3. Yu Z, Savinov R, Matura M, et al. (2025) Current research status on advanced lattice structures for impact and energy absorption applications: a systematic review. *Thin-Walled Struct* 215: 113490. https://doi.org/10.1016/j.tws.2025.113490
4. Chouhan G, Bidare P, Bala Murali G (2024) Triply periodic minimal surface based lattices for acoustic performance. *Noise Vib Worldw* 55: 454–468. https://doi.org/10.1177/09574565241270201
5. Habib C, Kwon YW, Sachau D, et al. (2025) Review and assessment of various lattice structure homogenization. *Multiscale Multidiscip Model Exp Des* 9: 55. https://doi.org/10.1007/s41939-025-01118-1
6. Udenni Gunathilake TMS, Ching YC, Ching KY, et al. (2017) Biomedical and microbiological applications of bio-based porous materials: a review. *Polymers* 9: 160. https://doi.org/10.3390/polym9050160
7. Liu J, Xu M, Zhang R, et al. (2022) Progress of porous/lattice structures applied in thermal management technology of aerospace applications. *Aerospace* 9: 827. https://doi.org/10.3390/aerospace9120827
8. Taub AI and Luo AA (2015) Advanced lightweight materials and manufacturing processes for automotive applications. *MRS Bull* 40: 1045–1054. https://doi.org/10.1557/mrs.2015.268
9. Zhang J, Shen Y, Sun Y, et al. (2022) Design and mechanical testing of porous lattice structure with independent adjustment of pore size and porosity for bone implant. *J Mater Res Technol* 18: 3240–3255. https://doi.org/10.1016/j.jmrt.2022.04.002
10. du Plessis A, Razavi N, Benedetti M, et al. (2022) Properties and applications of additively manufactured metallic cellular materials: a review. *Prog Mater Sci* 125: 100918. https://doi.org/10.1016/j.pmatsci.2021.100918
11. Rico-Baeza G, Pérez-Soto GI, Morales-Hernández LA, et al. (2023) Additively manufactured foot insoles using body-centered cubic (BCC) and triply periodic minimal surface (TPMS) cellular structures. *Appl Sci* 13: 12665. https://doi.org/10.3390/app132312665

12. Lyu Y, Gong T, He T, et al. (2024) Study on the energy absorption performance of triply periodic minimal surface (TPMS) structures at different load-bearing angles. *Biomimetics* 9: 392. https://doi.org/10.3390/biomimetics9070392
13. Cho J, Lee ES, Kim JH, et al. (2025) Design of lattice-based energy-absorbing structure for enhancing the crashworthiness of advanced air mobility. *Aerospace* 12: 332. https://doi.org/10.3390/aerospace12040332
14. Chouhan G and Bala Murali G (2024) Designs, advancements, and applications of three-dimensional printed gyroid structures: a review. *Proc Inst Mech Eng Part E J Process Mech Eng* 238: 965–987. https://doi.org/10.1177/09544089231160030
15. Gandhi R, Salmi M, Roy B, et al. (2025) Mechanical performance, fatigue behaviour, and biointegration of additively manufactured architected lattices. *Virtual Phys Prototyp* 20: e2530733. https://doi.org/10.1080/17452759.2025.2530733
16. Chouhan G (2024) Comparative study on tensile and morphological properties of resin and rice husk reinforced polymer composite gyroid lattice structures. *Eng Res Express* 6: 25543. https://doi.org/10.1088/2631-8695/ad4aec
17. Qiu N, Mou W, Yang J, et al. (2026) Mechanical performance of triply periodic minimal surface (TPMS) lattices under multiple loading conditions. *Thin-Walled Struct* 223: 114634. https://doi.org/10.1016/j.tws.2026.114634
18. Song W, Mu K, Feng G, et al. (2023) Mechanical properties of 3D printed interpenetrating phase composites with TPMS architectures. *Thin-Walled Struct* 193: 111210. https://doi.org/10.1016/j.tws.2023.111210
19. Shi W, Lin Y, Li J, et al. (2024) Optimization of mechanical properties of Ti–6Al–4V triply periodic minimal surface porous structures prepared by laser beam powder bed fusion technology based on orientation control. *Mater Sci Eng A* 894: 146183. https://doi.org/10.1016/j.msea.2024.146183
20. Carlsson J, Kuswoyo A, Shaikeea A, et al. (2024) Compression of filled, open-cell, 3D-printed Kelvin lattices. *Mech Mater* 188: 104851. https://doi.org/10.1016/j.mechmat.2023.104851
21. Wei Y, Li H, Ma Y, et al. (2025) Kelvin lattice structures fabricated by laser powder bed fusion: Design, preparation, and mechanical performance. *China Foundry* 22: 117–127. https://doi.org/10.1007/s41230-025-5007-z
22. Fauziah S and Amirpour M (2025) Fatigue behavior of 3D-printed solid liquid composite (SLC) orthotic insole: an experimental study. *Int J Adv Manuf Technol* 139: 5991–6008. https://doi.org/10.1007/s00170-025-16204-4
23. Chhikara K, Singh G, Gupta S, et al. (2022) Progress of additive manufacturing in fabrication of foot orthoses for diabetic patients: a review. *Ann 3D Print Med* 8: 100085. https://doi.org/10.1016/j.stlm.2022.100085
24. Cracknell D, Battley M, Fernandez J, et al. (2024) Fluid-filled lattices for responsive orthotic insoles. *Smart Mater Struct* 33: 115034. https://doi.org/10.1088/1361-665X/ad860c
25. Chibinyani M, Dzogbewu TC, Maringa M, et al. (2024) Natural cellular structures in engineering designs built via additive manufacturing. *Mater Technol* 40: 2443211. https://doi.org/10.1080/10667857.2024.2443211
26. Williams C (2008) Design and development of a layer-based additive manufacturing process for the realization of metal parts of designed mesostructure[PhD thesis], USA: Georgia Institute of Technology.

27. Khan K, Hussain MI, Tareen AK, et al. (2026) Advances in vat photopolymerization 3D printing: Multifunctional materials, process innovations, and emerging applications. *Mater Sci Eng R Reports* 167: 101120. https://doi.org/10.1016/j.mser.2025.101120
28. Xu S, Huang C, Liu H, et al. (2026) Vat photopolymerization additive manufacturing for advanced ceramics: techniques, multimaterial strategies, and applications. *Adv Eng Mater* 28: e202501811. https://doi.org/10.1002/adem.202501811
29. Ali F, Kalva SN, Koc M (2024) Advancements in 3D printing techniques for biomedical applications: a comprehensive review of materials consideration, post processing, applications, and challenges. *Discov Mater* 4: 53. https://doi.org/10.1007/s43939-024-00115-4
30. Hozdić E (2024) Characterization and comparative analysis of mechanical parameters of FDM- and SLA-printed ABS materials. *Appl Sci* 14: 649. https://doi.org/10.3390/app14020649
31. Li D, Liao W, Dai N, et al. (2019) Comparison of mechanical properties and energy absorption of sheet-based and strut-based gyroid cellular structures with graded densities. *Materials* 12: 2183. https://doi.org/10.3390/ma12132183
32. Dias Gonçalves VP, Vieira CMF, Simonassi NT, et al. (2024) Evaluation of mechanical properties of ABS-like resin for stereolithography versus ABS for fused deposition modeling in three-dimensional printing applications for odontology. *Polymers* 16: 2921. https://doi.org/10.3390/polym16202921
33. Watters MP and Bernhardt ML (2018) Curing parameters to improve the mechanical properties of stereolithographic printed specimens. *Rapid Prototyping J* 24: 46–51. https://doi.org/10.1108/RPJ-11-2016-0180



AIMS Press

© 2026 the Author(s), licensee AIMS Press. This is an open access article distributed under the terms of the Creative Commons Attribution License (https://creativecommons.org/licenses/by/4.0)